Stability considerations of unequal-leg angle stainless steel columns

Max E. Laracuente[1], Edward J. Sippel[2], Hannah B. Blum[3]

Abstract

Due to limited research, design guidelines for stainless steel single-angle compression members in the recently released AISC 370: Specification for Structural Stainless Steel Buildings are currently limited to equal-leg sections and require the consideration of flexural-torsional stability in contrast to the previous Design Guide 27 recommendations. This paper reports on the ongoing experimental and numerical investigation on the stability considerations of unequal-leg angle stainless steel columns. A series of unequal-leg angles with cross-sectional dimensions of 3" x 2" x ¼" and lengths ranging from 10 to 100 inches were tested in compression. From these tests the ultimate loads were recorded in addition to displacements, twists, and failure modes through the use of strain gauges and an optical tracking system. The material properties were obtained through a series of tensile coupon tests, and the member geometric imperfections were measured through a non-contact 3D laser scanning technique. The data obtained from these tests will be used to validate a finite element model of the unequal-leg angles, which will be utilized in an upcoming parametric study to obtain numerical capacities and failure modes for various geometrical parameters. The results obtained from this ongoing investigation will serve to inform design requirements for unequal-leg angles in compression including evaluating the requirement to consider flexural-torsional stability.

1. Introduction

The recent release of American Institute of Steel Construction (AISC) Specification for Structural Stainless Steel Buildings (AISC, 2021) has provided additional opportunities to implement stainless steel members and take advantage of corrosion resistance, thermal properties, and aesthetics among other benefits (Houska, 2014). The Specification provides an updated design procedure to evaluate members in compression including compact, equal-leg single angles. Unlike carbon steel members designed according to AISC 360 (AISC, 2016), the stainless steel provisions incorporate a three stage buckling model that separates the response into full member yield, inelastic buckling, and elastic buckling. Another modification to the design procedure is the consideration of flexural-torsional buckling with single angles. The design provisions for carbon steel single angles permit

---

[1]Graduate Research Assistant, University of Wisconsin-Madison, <mlaracuente@wisc.edu>
[2]Graduate Research Assistant, University of Wisconsin-Madison, <esippel@wisc.edu>
[3]Assistant Professor and Alain H. Peyrot Fellow, University of Wisconsin-Madison, <hannah.blum@wisc.edu>

excluding the direct calculation of flexural-torsional buckling, unless the legs are highly slender, since the local buckling reduction adequately reduces the flexural buckling capacity. Galambos (1991) demonstrated how this combination of flexural and local buckling results in the safe design of single angles. Previous design recommendations for stainless steel, provided in the 2013 edition of Design Guide 27 (Baddoo, 2013), were formulated following the carbon steel provisions and extended the same exception to stainless steel single angles. While some variations exist between the previous and current approaches, one consistent factor is that unequal-leg angles are beyond the scope of the design procedures due to limited relevant research.

In recent years, a growing amount of research on stainless steel equal-leg angles subjected to uniform compression has been completed. Early stub column tests of austenitic cold-formed angles by Kuwamura (2003) captured failure at greater than nominal yield stresses by flexural-torsional buckling for short columns. Sun et al. (2019) captured a similar response with hot-rolled stub column tests incorporating multiple grades. Various researchers have completed experiments capturing flexural-torsional buckling at shorter spans and flexural buckling for longer lengths including duplex laser-welded angles (Reynolds, 2013); austenitic laser-welded angles (Filipović, Dobrić, Buđevac, et al., 2021); austenitic cold-formed angles (Dobrić et al., 2020; Zhang, Tan, and Zhao, 2019); and austenitic hot-rolled angles (de Menezes et al., 2019; Sarquis et al., 2020; Behzadi-Sofiani, Gardner, and Wadee, 2021; Filipović, Dobrić, Baddoo, et al., 2021). Comparisons to existing design provisions including Design Guide 27 have found that the existing design provisions were conservative, especially for short columns exhibiting flexural-torsional buckling (Zhang, Tan, and Zhao, 2019; Sarquis et al., 2020; Dobrić et al., 2020; Behzadi-Sofiani, Gardner, and Wadee, 2021; Filipović, Dobrić, Baddoo, et al., 2021; Filipović, Dobrić, Buđevac, et al., 2021).

Despite the increase in data for equal-leg angles, only minimal existing research on unequal-leg angles subjected to uniform compression, and none for stainless steel members, was located. Early work by Liu and Chantel (2011) considered 26 carbon steel unequal-leg angles subjected to compression with varying amounts of eccentricity. All five concentrically loaded angles failed primarily in flexural buckling at less than 40% of the yield stress. Dinis et al. (2015) evaluated four carbon steel unequal-leg angles to investigate the elastic flexural-torsional response in asymmetric sections. Experimental results and subsequent modeling were found to be in agreement with the standard theoretical elastic buckling capacity used in the AISC Specifications. Ojalvo (2011) summarized the results of three fixed end aluminum unequal-leg angles tests (Liao, 1982; Wu, 1982). As noted by Dinis et al. (2015), the inelastic response of the fixed ended columns captured additional post-critical strength excluded in the standard elastic buckling assumptions. Recently, Zhang, Wang, et al. (2020) and Zhang, Bu, et al. (2021) tested 22 pinned end aluminum unequal-leg angle columns. Experimental results consistently exhibited flexural-torsional buckling; however, the response was dominated by torsional behavior at short lengths with a gradual transition to significant flexural behavior at long lengths.

This paper summarizes the progress on an ongoing study of stainless steel unequal-leg angles subjected to concentric compression. The goal is to expand the limited research on the behavior of this asymmetric shape and to inform design requirements for stainless steel unequal-leg angles in compression. The study also evaluates the current AISC 370 design requirement of considering flexural-torsional stability across all lengths.

Table 1: Chemical composition of tested stainless steel angles

Chemical Composition (Weight %)											
	C	Si	Mn	P	S	Cr	Mo	Ni	Cu	Ti	Co	N
Min.	-	-	-	-	-	18.00	-	8.00	-	-	-	-
Max.	0.030	0.75	2.00	0.040	0.030	19.60	1.00	10.00	1.00	-	-	0.1000
Results	**0.027**	**0.49**	**1.87**	**0.035**	**0.003**	**18.15**	**0.19**	**8.02**	**0.46**	**-**	**-**	**0.0670**

Table 2: Measured geometric properties of test specimens

Specimen	L (in)	b (in)	h (in)	t_b (in)	t_h (in)	Area (in^2)
S10-A1-1	10	2.049	2.979	0.257	0.266	1.251
S10-A2-1	10	2.055	2.977	0.258	0.243	1.191
S10-A2-2	10	2.052	2.966	0.258	0.244	1.192
S20-A1-1	20	2.030	2.981	0.253	0.253	1.203
S20-A2-1	20	2.063	2.958	0.258	0.241	1.182
S20-A2-2	20	2.063	2.965	0.259	0.243	1.190
S36-A1-1	36	2.019	2.985	0.251	0.253	1.198
S36-A1-2	36	2.014	2.991	0.251	0.253	1.198
S36-A2-1	36	2.076	2.964	0.259	0.241	1.190
S72-A5-1	72	2.005	2.987	0.250	0.250	1.185
S72-A5-2	72	2.010	2.985	0.251	0.249	1.184
S72-A6-1	72	2.034	2.980	0.253	0.256	1.214
S100-A3-1	100	2.057	2.957	0.258	0.252	1.210
S100-A4-1	100	2.067	2.933	0.258	0.252	1.208
S100-A4-2	100	2.063	2.939	0.258	0.253	1.209
S148-A1-1	147.9375	2.006	2.999	0.249	0.254	1.199
S148-A2-1	147.9375	2.033	2.972	0.256	0.244	1.182
S148-A3-1	147.9375	2.020	2.989	0.255	0.254	1.210

2. Experimental Investigation

2.1 General

The ongoing experimental investigation focuses on testing unequal-leg stainless steel angles under axial compression through failure to approximately 80% post ultimate load. The experimental investigation involved material tensile coupon tests, initial geometric imperfection measurements, and member tests on ten fixed-end unequal-leg stainless steel angles with varying lengths. All specimens were cut from six different 21 foot-long pieces, which were labeled A1 to A6. They were given a unique name which identifies the nominal length, the angle it was cut from, and the number. For example, with specimen S10-A2-2, 'S10' represents a specimen with a 10" length, 'A2' represents the specimen was cut from piece A2, and '2' represents this is the second 10" specimen cut from piece A2. The tested cross section was a hot-rolled 3" x 2" x ¼" angle in Grade 304 austenitic stainless steel. The chemical composition of the tested material, as reported in the manufacturer's mill certificate, is presented in Table 1. The measured geometric properties of the specimens used in this study are shown in Table 2, where L is the length of the specimen, b and h are the width and height of the section, respectively, t_h is the thickness of the 3" leg, and t_b is the thickness of the 2" leg as depicted in Fig. 1.
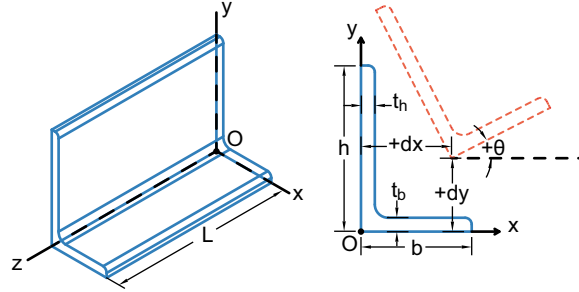
Figure 1: Unequal-leg angle conventions for dimensions, axes, and displacements

Table 3: Experimental mechanical properties

Specimen	E (ksi)	f_y (ksi)	$f_{1.0}$ (ksi)	n	$n_{0.2,1.0}$
SC10-1	28745	52.6	64.7	5.35	2.57
SC10-2	27779	38.9	50.9	4.23	2.20
SC10-3	28353	43.4	46.2	10.45	1.51
SC18-1	25755	54.9	63.5	8.78	2.12
SC18-2	27799	54.5	62.3	9.13	2.55
SC18-3	27757	46.1	53.7	8.83	2.29
Average	**27698**	**48.4**	**56.9**	**7.80**	**2.21**
Nominal	28000	30	–	7	–

2.2 Tensile coupon test

Prior to the column compression tests, a series of tensile coupon tests were performed to obtain the material properties of the studied stainless steel angle section. One coupon was cut from the middle portion of the 2" leg and two coupons were cut from the 3" leg in the longitudinal direction (see Fig. 2). All coupons were cut from from either a 10" segment from A2 or an 18" segment from A5. The coupons were all given a unique name which identifies the angle it was cut from and the number. For example, with coupon SC10-2, 'SC10' represents a coupon cut from the 10" piece, and '2' represents this is the second coupon cut from the 10" piece. The coupon dimensions were chosen to meet the requirements specified in the ASTM E8/E8M-16a (2016). A total of 6 tensile tests were conducted using (i) an MTS Criterion 43 with a 50-kN capacity and (ii) an MTS 810 Servo-Hydraulic frame with a 100-kip capacity. For the coupons tested on the MTS Criterion 43, two linear electrical resistance strain gauges were attached at mid-height to the center of the front and back faces of the coupons to determine the strains in the longitudinal direction. In addition, an extensometer with a 2" gauge length was used to obtain the average strain over the gauge length. For the coupons tested on the MTS 810 Servo-Hydraulic frame, only the 2" gauge length extensometer was used to record the strains. Two different machines were used because the MTS 810 Servo-Hydraulic frame did not have the capacity of providing three outputs and the MTS Criterion 43, which allowed three outputs, did not have the capacity to run the test up to ultimate and fracture. Thus a combination was used to ensure adequate data capture in the elastic range and at ultimate. The engineering stress-strain curves obtained from the tensile coupon tests are shown in Fig.2. This plot contains a legend which shows the location in the cross-section where each tensile coupon was cut. These curves represent static material properties and were obtained
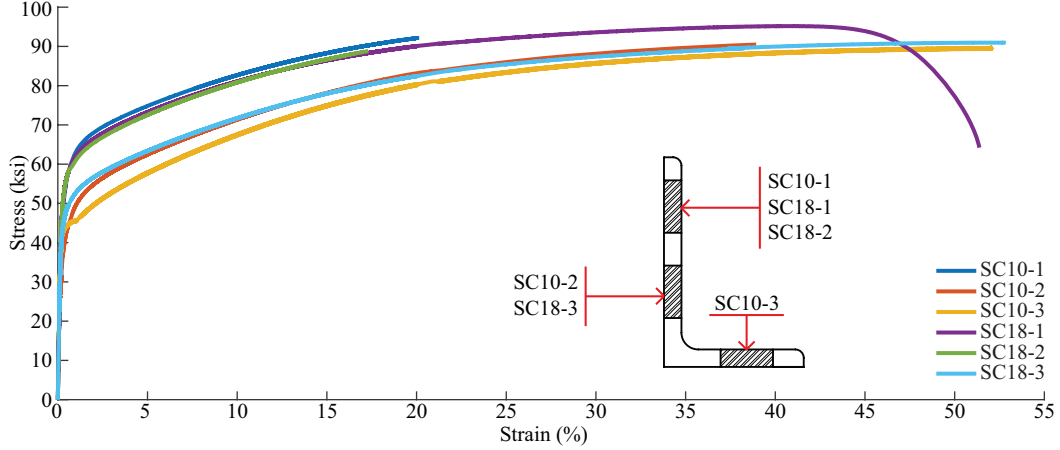
4

Figure 2: Measured stress-strain curves from coupon tests

following the procedure proposed by Huang and Young (2014). From the stress-strain plot a pattern can be seen were coupons that were taken from the edge of the 3" leg had higher stress values than the coupons taken near the heel of that same leg or the 2" leg. The mechanical properties obtained from these tests are presented in Table 3, where E is the Young's modulus, f_y and $f_{1.0}$ are the 0.2% and 1.0% proof stresses, respectively, and n and $n_{0.2,1.0}$ are the Ramberg–Osgood strain hardening exponents, with $n_{0.2,1.0}$ corresponding to a model proposed by Arrayago et al. (2015).

2.3 Initial Geometric Imperfection Measurements

The initial geometric imperfections of the specimens were measured through a non-contact 3D laser scanning technique using the Artec Leo Scanner. The angles were scanned in three orientations to create a 3D point cloud of the complete surface. Reconstruction of the data in Artec Studio 15 (Artec 3D, 2020) was aided by the use of a background with unique texture and geometry created from metal decking and various markings on the angle itself as shown in Fig. 3. Post-processing of the data established the coordinates of the angle heel and inclination of each leg (twist) along the length of the member through linear-fits of the exterior face of the angle referencing Zhang et al.'s work (2021). The imperfection along the length of the member, dx and dy in the x- and y- direction, respectively, were determined based on Eq. 1 where (x, y) are the coordinates of the heel, i is the current cross section along the length z of the member, and n is the total number of cross sections as shown in Fig. 1;

$$[dx, dy]_i = \left[x_i - x_1 + (x_n - x_1)\frac{i-1}{n-1}, y_i - y_1 + (y_n - y_1)\frac{i-1}{n-1} \right] \quad (1)$$

Table 4 summaries the maximum imperfection measured along the length of each member with a typical example shown in Fig. 4.
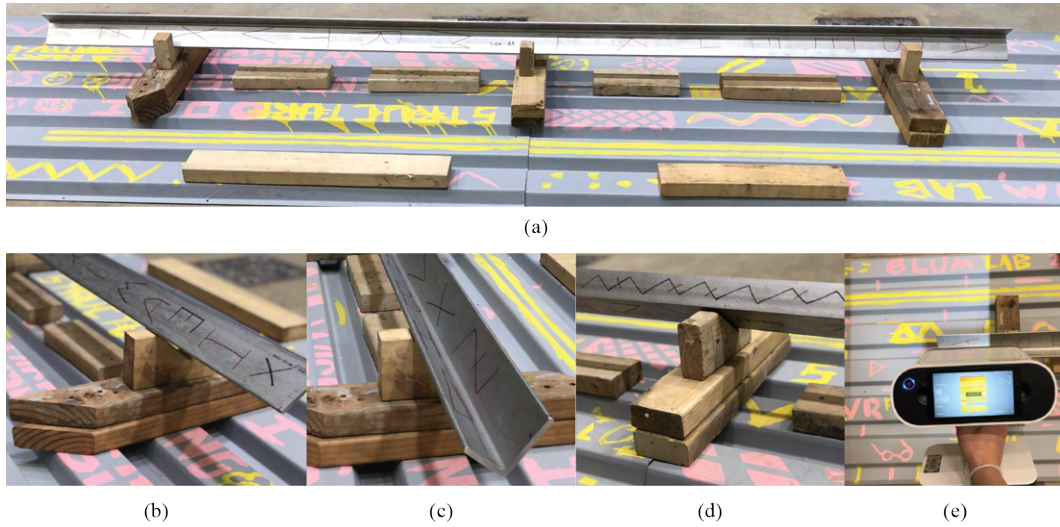
5

Figure 3: Imperfection scanning process. (a) Overview of angle to be scanned on background (b) Angle positioned to scan complete exterior face (c) Angle positioned to scan complete interior face (d) Angle positioned to scan majority of both faces at same time (e) Leo scanner capturing data of background and angle. Credit to the Blum research group for excellent painting of the steel deck to assist the scanner with tracking.
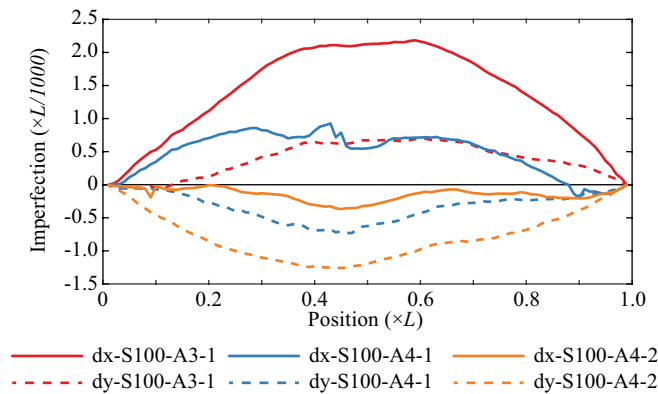

Figure 4: Initial imperfection of the 100" specimen

Table 4: Maximum measured imperfection

Specimen	dx		dy	
	(in)	(×L/1000)	(in)	(×L/1000)
S10-A1-1	-0.014	-1.434	-0.007	-0.705
S10-A2-1	0.003	0.347	0.002	0.197
S10-A2-2	0.003	0.300	0.002	0.150
S20-A1-1	-0.016	-0.787	-0.013	-0.639
S20-A2-1	-0.006	-0.288	-0.003	-0.160
S20-A2-2	0.005	0.236	-0.009	-0.442
S36-A1-1	0.018	0.494	-0.018	-0.499
S36-A1-2	-0.011	-0.299	-0.036	-1.000
S36-A2-1	-0.048	-1.339	-0.022	-0.603
S72-A5-1	0.063	0.873	-0.064	-0.893
S72-A5-2	-0.142	-1.978	-0.134	-1.857
S72-A6-1	0.035	0.483	-0.037	-0.520
S100-A3-1	0.218	2.183	0.070	0.695
S100-A4-1	0.086	0.858	-0.073	-0.732
S100-A4-2	-0.037	-0.369	-0.126	-1.259
S148-A1-1	-0.070	-0.472	-0.141	-0.955
S148-A2-1	0.470	3.178	0.206	1.389
S148-A3-1	0.287	1.943	-0.070	-0.474

2.4 Column Buckling Test

2.4.1 Test-setup

Ten 3" x 2" x ¼" hot-rolled Grade 304 austenitic stainless steel unequal-leg angles, with varying lengths from 10" to 100", were tested in compression to quantify their buckling response and load-carrying capacity. All tests were conducted in a Southwark Emery Testing Machine with a capacity of 1 million pounds in tension and compression. The applied load was measured by means of a 100 kip load cell attached to the cross head of the testing machine. All tests were performed in a displacement control mode with a constant axial displacement rate of 0.0015 in/min. This rate allowed the specimens be tested under quasi-static conditions. The strain gauges at each end were used to align the member while subjecting the specimen to an initial 2 kip preload. All tests were stopped when the load reached 80% post-peak. The average strains at mid-height were determined by using two linear electrical resistance strain gauges attached to the center of the front and back faces of both legs. Displacements and twists were recorded through an optical tracking system with an overall accuracy of 0.004 in. A total of two optical tracking system markers were placed in the outside face of each leg near the ends, at quarter points, and at mid-span for the majority of the tests performed; for the smaller lengths a reduced number of markers were used. The configuration of the strain gauges and the optical tracking system markers at mid-height are shown in Fig.5.

To achieve fixed boundary conditions, the ends of the angle were restrained by fabricated steel plates (see Fig. 6) similar to the setup of Zhang et al. (2019). This method simplifies the testing process due to the simplicity of exchanging specimens between tests. While the bottom plate was directly on the floor, the top plate was bolted to a thicker plate which was connected to the load
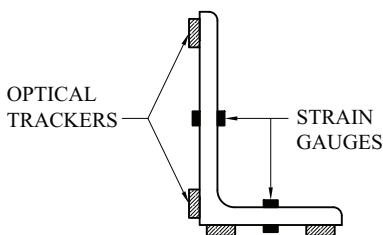
Figure 5: Position of the optical trackers and strain gauges

Figure 6: End plates used to achieve fixed boundary conditions

cell, and this was gripped to the cross head of the testing machine. Both top and bottom plates were aligned with the centroid of the unequal-leg angle cross-section to ensure pure axial compression. The column buckling test setup is presented in Fig.7.

2.4.2 Results

The failure loads obtained from all tests are summarized in Table 5; the remaining two columns will be addressed in Section 3. The majority of the pairs tested had a similar maximum load with a difference ranging from 1-2%. However, both 10" specimens and 72" specimens had a difference in the maximum load of 11% and 32%, respectively. This difference in maximum load for both specimens could be due to the high difference in their measured initial imperfections. Table 4 shows that specimen S10-A1 had an imperfection approximately 4.5 times bigger in the x-direction and 3.5 times bigger in the y- direction than specimen S10-A2-1. Specimen S72-A5-2 had an imperfection approximately 4 times bigger in the x- direction and 3.5 times bigger in the y-direction than its pair S72-A6.

Figs. 8 - 11 illustrate a graphical representation of the results obtained from the compression tests of one 20" and both 36", 72", and 100" specimens. These plots quantify how much each specimen displaced laterally, in the x- and y-directions, and how much they twisted at mid-height. The
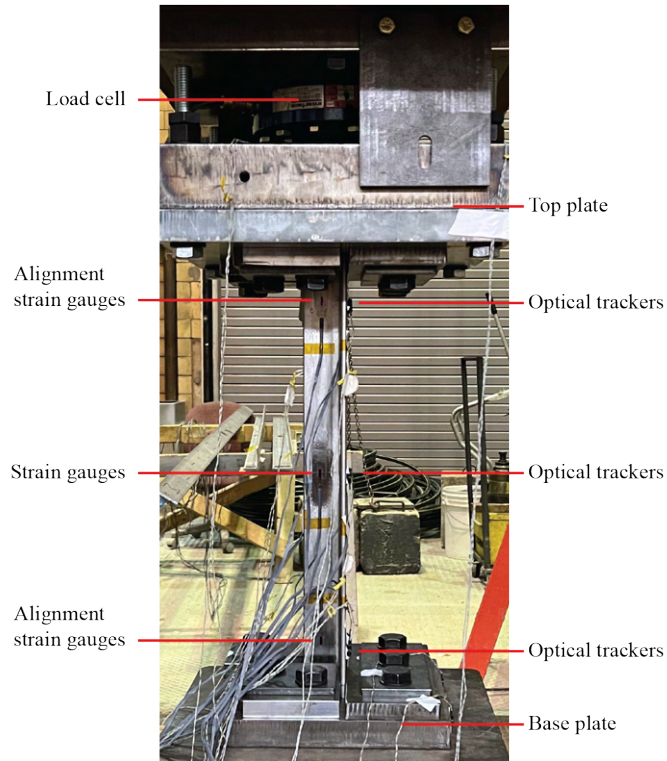
8

Figure 7: Typical test set-up

displacements and twists for both 10" specimens and one 20" specimen are not presented in this paper due to a malfunction of the optical tracking system in all three tests. The coordinate system used for these measurements contains the origin at the heel of the angle, with the x-axis parallel to the 2" leg and the y-axis parallel to the 3" leg. Fig. 1 provides a visual representation of the selected coordinate system and the sign convention used for all tests. In order to compare the nominally identical specimens, corresponding results were plotted on the same figure. The plots for the 36" and 100" specimens show that all tests performed on specimens of the same size obtained similar results. The plots for both 72" specimens show the displacements and twist moving in different directions because both specimens buckled in opposite directions. Despite this difference, both specimens had a maximum displacement when the test was terminated at 80% post-peak in the x- and y-direction of approximately 1" and 0.4" respectively. The biggest difference is in the rotation of the specimen with one being approximately 2.75° and the other -4.75°; this corresponds to a 53% difference. The plots for both 100" specimens show that after peak-load was reached, a sudden loss in the strength capacity of both members occurred; this behavior was observed only with these specimens. Also, these plots show a black dashed line from the origin to approximately 2 kip; it represents an interpolation of the data in this region. As mentioned in Section 2.4.1, all specimens were preloaded to verify alignment. For the majority of the tests the preload decreased with time before data recording began, but for the 100" specimens the preload did not decrease. Therefore, the collection of data started approximately at 2 kip. In general, Figs. 9 - 11 show that there is good agreement in the overall results obtained from identical length specimens.

Fig. 12 shows the position of a cross section at mid-height at the start of the test, peak load, and

9

Table 5: Experimental failure loads compared to design loads using nominal and measured material properties

Specimen	Load (kip)	Load/$P_{d,nom}$	Load/$P_{d,meas}$
S10-A1-1	62.1	2.035	1.405
S10-A2-1	69.5	2.278	1.573
S20-A2-1	66.8	2.353	1.662
S20-A2-2	65.4	2.304	1.628
S36-A1-2	52.7	1.985	1.432
S36-A2-1	53.3	2.008	1.449
S72-A5-2	24.8	1.289	1.029
S72-A6-1	34.4	1.787	1.427
S100-A4-1	18.4	1.324	1.170
S100-A4-2	18.0	1.295	1.145

80% post-peak load of a short, mid and long length specimen. These plots show that all tested specimens failed in three different modes: (i) torsional mode, (ii) flexural mode, and (iii) flexural-torsional mode. At the shorter lengths, 10" and 20" specimens, it was observed that there are no significant lateral displacements and the biggest movements were rotations (see Fig. 12(a)). At the 36" length, both tests showed a consistent behavior where the torsional mode was reduced as compared to the shorter lengths, and the flexural mode began to participate in the overall failure mode (see Figs. 12(b) & 12(c)). The 72" specimens showed that rotations were once again reduced and the lateral displacements continued to increase relative to the shorter lengths, indicating that the flexural mode had a major participation in the overall failure mode (see Figs. 12(d) & 12(e)). At the 100" length, the flexural mode had the biggest participation in the overall behavior of the section due to some significant lateral displacements and small rotations when compared to the shorter specimens (see Figs. 12(f) & 12(g))). When comparing all the data obtained from the experimental investigation it was observed that torsional buckling is dominant in the shorter lengths and flexural buckling in the longer lengths, with a transition occurring gradually in the middle lengths. Fig. 13 illustrates some photographs taken during the compression tests performed on the various stainless steel angles.

3. Buckling Load Discussion

The compression member design provisions for single angles according the AISC 370-21 require that flexural buckling as well as flexural-torsional buckling are considered. No matter which behavior is determined to control the buckling response, the elastic buckling stress is converted to the critical buckling stress by the same relationship developed primarily based on flexural buckling results (Meza, Baddoo, and Gardner, 2021). It has been shown that this procedure is conservative for carbon steel single angles, in part, due to shear stiffness not decreasing under compression loading unlike longitudinal stiffness, and alternatively the buckling capacity of single angles can be safely designed by considering flexural buckling with local buckling reductions for noncompact sections (Galambos, 1991; Galambos, 1963; Kitipornchai and Lee, 1986; Trahair and Kitipornchai, 1972). Galambos (1991) demonstrated how different stiffness reductions for shear and longitudinal behavior could combine into a single equation representing the full design provisions, which was implemented in work by Sippel et al. (2022). The standard elastic buckling relationship can be modified to determine the inelastic critical buckling stress, f_{in}, as shown in Eq. 2;
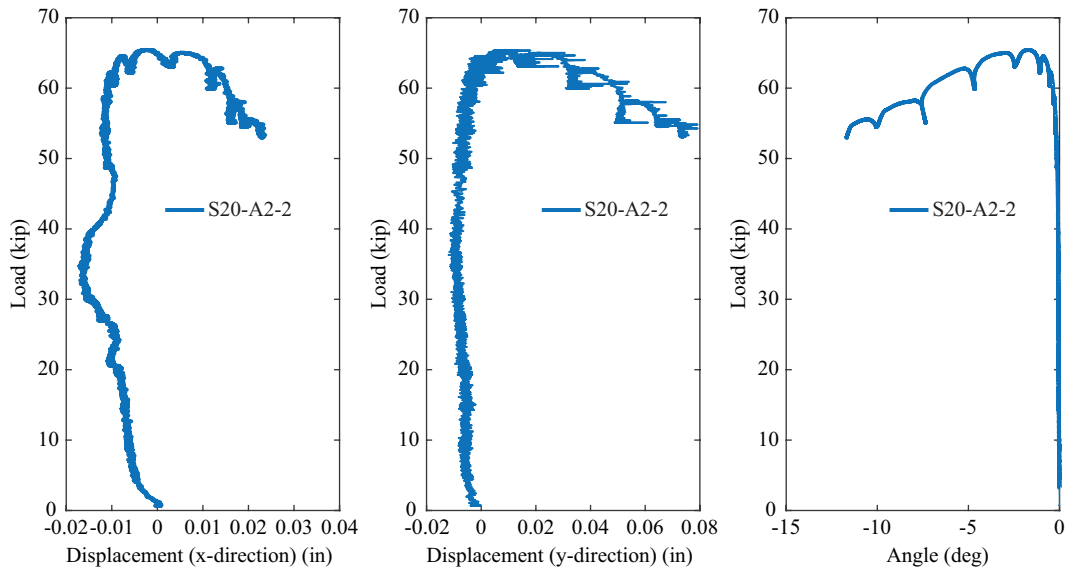
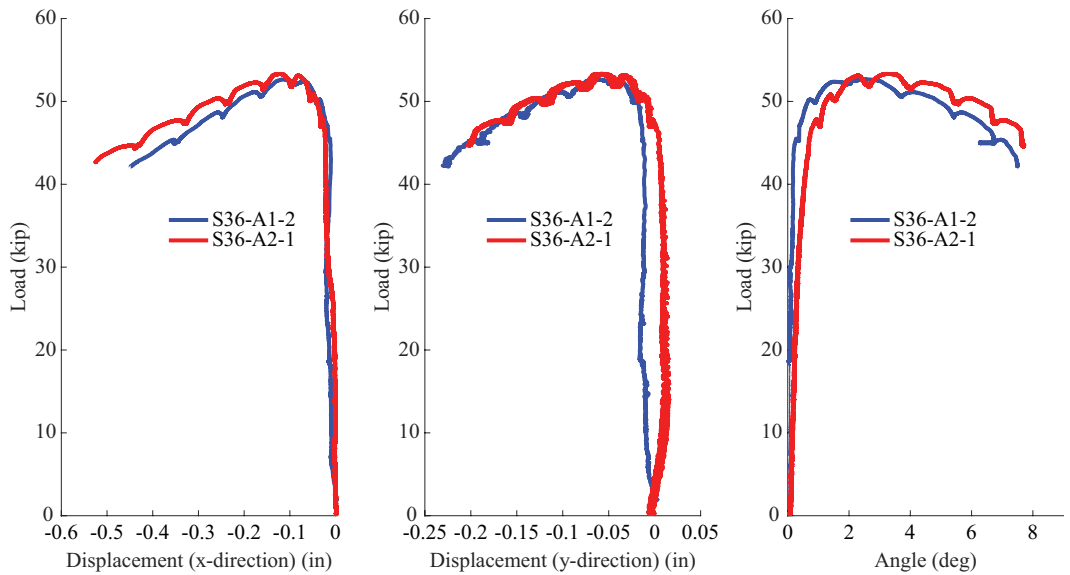Figure 8: Displacement and rotations obtained for one 20" angle

Figure 9: Displacement and rotations obtained for both 36 inch angle
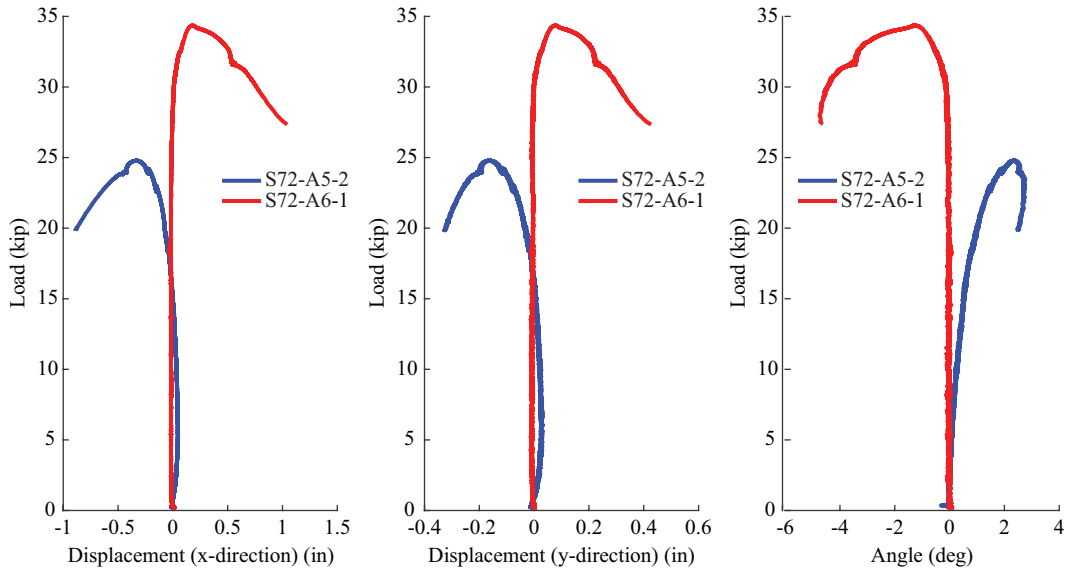
11

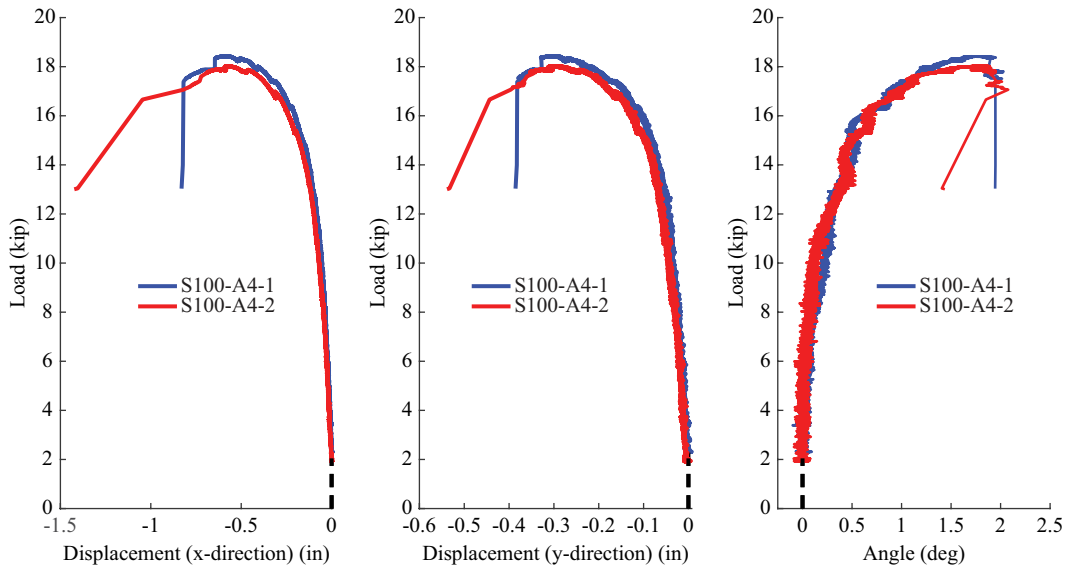Figure 10: Displacement and rotations obtained for both 72 inch angle

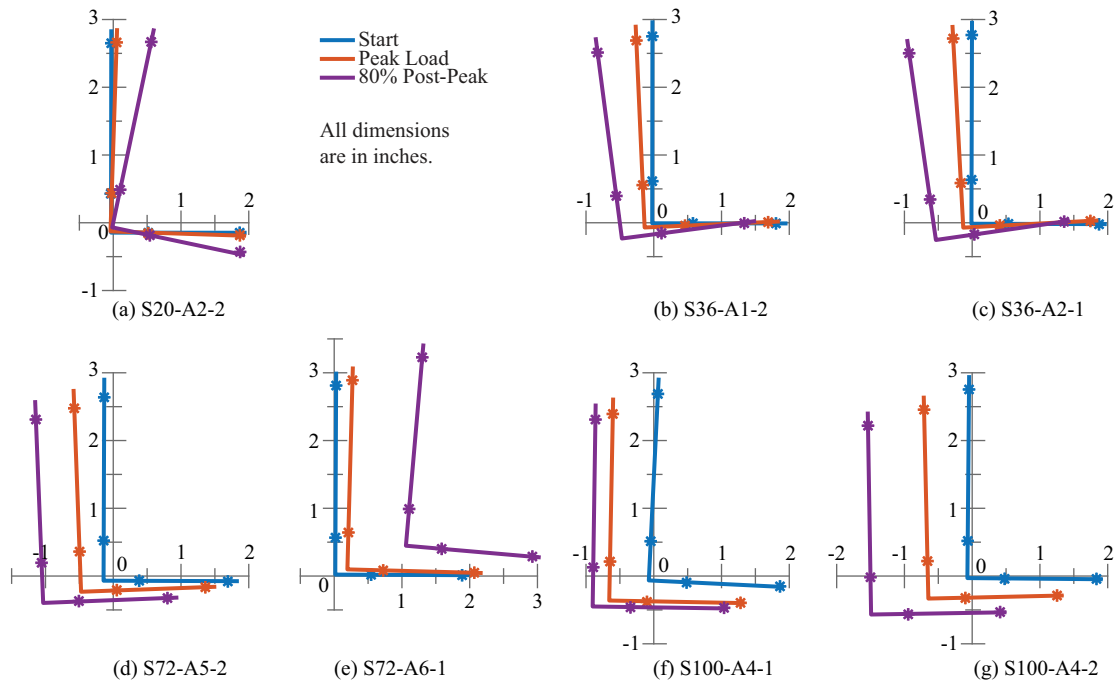Figure 11: Displacement and rotations obtained for both 100 inch angle

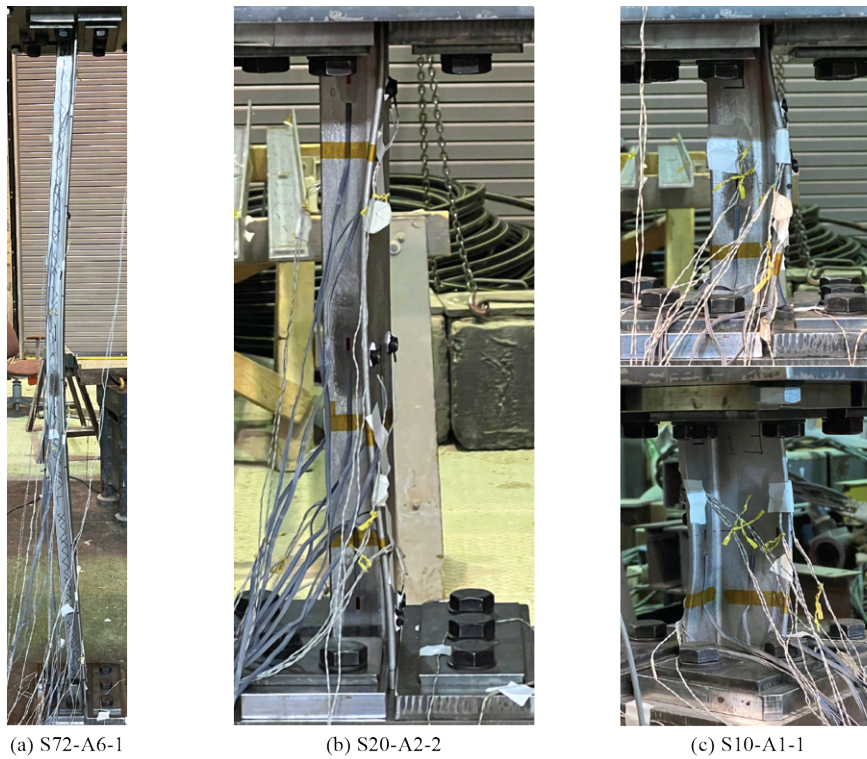Figure 12: Cross-section position at start, peak load, and 80% post-peak of various specimens

Figure 13: Photographs of buckled specimens

$$\left(f_{in} - f_{xb}\tau\right)\left(f_{in} - f_{yb}\tau\right)\left(f_{in} - \frac{\tau_G GJ + \tau\pi^2 EC_w/L^2}{r_0^2}\right)$$
$$-f_{in}^2\left(f_{in} - f_{yb}\tau\right)\frac{x_0^2}{r_0^2} - f_{in}^2\left(f_{in} - f_{xb}\tau\right)\frac{y_0^2}{r_0^2} = 0 \tag{2}$$

where $f_{xb} = \pi^2 EI_x/\left(L^2 A\right)$ and $f_{yb} = \pi^2 EI_y/\left(L^2 A\right)$ are the critical flexural buckling stresses about the principal x- and y-axis, respectively, I_x and I_y are the moments of inertia about the principal x- and y-axis, A is the cross-sectional area, J is the torsion constant, C_w is the warping constant, G is the shear modulus, L is the effective length, τ and τ_G are the stiffness reduction factors for longitudinal and shear stiffness, $r_0 = \sqrt{\left(I_x + I_y\right)/A + x_0^2 + y_0^2}$ is the polar radius of gyration about the shear center, and (x_0, y_0) are the coordinates of the shear center relative to the centroid.

Similar to the study in Sippel et al. (2022), it is possible to evaluate Eq. 2 for any effective longitudinal stiffness relationship to define the τ factor. For stainless steel, two relationships of interest are the current AISC stainless steel design provisions for compression members and the stress-strain relationship. The three-stage buckling relationship in the Specification can be rearranged to define the design longitudinal stiffness reduction factor, $\tau_{E,D}$, as shown in Eq. 3;

$$\tau_{E,D} = \begin{cases} \beta_2 & \text{if } \frac{f_{in}}{f_y} \leq \beta_2/3.20 \\ \frac{f_{in}}{f_y}\left(\frac{\ln\left(f_{in}/(1.2f_y)\right)}{\ln \beta_1}\right)^{1/\alpha} & \text{otherwise} \end{cases} \tag{3}$$

where α, β_0, β_1, and β_2 are buckling coefficients provided for the Specification. For unequal-leg single angles, the values are given as $\alpha = 0.56$, $\beta_0 = 0.759$, $\beta_1 = 0.409$, and $\beta_2 = 0.690$. Missing from Eq. 3 is the constraint that the critical buckling stress cannot exceed f_y. Instead, the f_{in} was calculated assuming the inelastic behavior of $\tau_{E,D}$ applied for all short members and results were then reduced to the minimum of f_{in} and f_y. The Ramberg-Osgood stress-strain relationship introduced in Section 2.2 can be rearranged to define the stress-strain longitudinal stiffness reduction factor, $\tau_{E,SSC}$, as shown in Eq. 4;

$$\tau_{E,SSC} = \begin{cases} f_y/\left(f_y + 0.002En\left(\frac{f_{in}}{f_y}\right)^{n-1}\right) & \text{if } f_{in} \leq f_y \\ \frac{E_{t,y}}{E}f_r/\left(f_r + E_{t,y}\left(\epsilon_{max} - 0.002 - \frac{f_y}{E} - \frac{f_r}{E_{t,y}}\right)n_{0.2,max}\frac{f_{in}-f_y}{f_r}^{n_{0.2,max}-1}\right) & \text{otherwise} \end{cases} \tag{4}$$

where $E_{t,y} = E/\left(1 + 0.002nE/f_y\right)$ is the tangent modulus at f_y. As AISC and this paper utilize different reference stresses for the second stage of the stress-strain equation, generic parameters were introduced where f_{max} is the maximum stress, ϵ_{max} is the maximum strain, $n_{0.2,max}$ is the Ramberg-Osgood strain-hardening coefficient for the second stage, and $f_r = f_{max} - f_y$ is the reference stress range. The specific variables substituted for each relationship are provided in Table 6.

Table 6: Specific Ramberg-Osgood parameters for different models

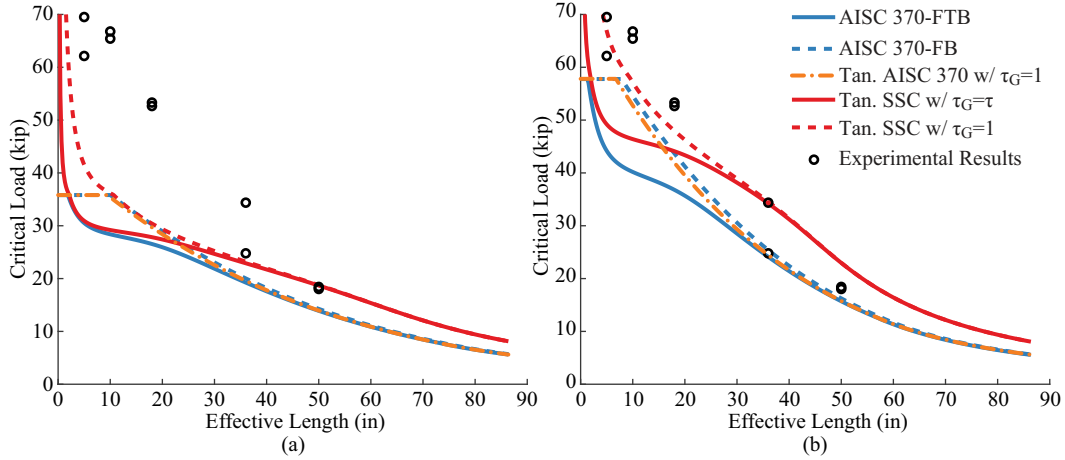| Model	f_{max}	ϵ_{max}	$n_{0.2,max}$
Nominal AISC	f_u	ϵ_u	m
Current Study	$f_{1.0}$	$\epsilon_{1.0}$	$n_{0.2,1.0}$

Figure 14: Comparing design provisions, tangential buckling, and test results. (a) Nominal F_y and stress-strain curve. (b) Measured average F_y and stress-strain curve

As noted above, the shear stiffness can have its own distinct relationship. While carbon steel and stainless steel have a different mechanical behavior, the equivalence of a partially yielded section and an initial linear-elastic response under a small torque presented by Neal (1950) would still be applicable. As such, a reasonable approximation for an upper bound is $\tau_G = 1$ indicating there is no shear stiffness reduction due to axial compression. On the other extreme, a lower bound assuming the same reduction for E and G, $\tau_G = \tau$, would indicate the relationship between E and G remains constant, matching the current design procedure.

These stiffness relationships allow for the comparison of the current design provisions, the buckling strength considering the stress-strain relationship, and the experimental results. The design provisions for compression members were directly evaluated to determine the buckling capacity when considering flexural-torsional buckling, labeled 'AISC 370-FTB', and evaluated again neglecting flexural-torsional buckling as done for carbon steel single angles, labeled 'AISC 370-FB'. Using Eq. 2 with $\tau_{E,D}$ and $\tau_G = 1$, the buckling capacity was determined considering flexural-torsional buckling while implementing the longitudinal tangent stiffness defined for design and without shear stiffness reduction from compression, labeled 'Tan. AISC 370 w/ $\tau_G = 1$'. The alternative condition of $\tau_G = \tau_{E,D}$ was not calculated as it is equivalent to the flexural-torsional buckling values using the Specification. Using Eq. 2 with $\tau_{E,SSC}$, the buckling capacities based on the stress-strain relationship were calculated for both values of τ_G with the results labeled 'Tan. SSC w/ $\tau_G = 1$' and 'Tan. SSC w/ $\tau_G = \tau$', respectively. The buckling capacities were evaluated considering both the nominal strength, as shown in Fig. 14(a), and the average measured strength listed in Table 3, as shown in Fig. 14(b). The nominal material behavior taken from AISC 370-21 (2021) considered $E = 28,000$ ksi, $f_y = 30$ ksi, $f_u = 75$ ksi, $\epsilon_u = 0.4$, $n = 7$, and $m = 2.12$.

A benefit of this comparison is that it can be observed how the simplified design equations relate to the measured nonlinear behavior of stainless steel. The stress-strain response does not account for imperfections and all residual stress effects, but would serve as an estimate of the upper limit of the expected behavior. Similar behavioral trends were observed between the design and the stress-strain buckling values after accounting for the different assumptions on shear behavior. For short members, it is noted that the design buckling capacity approaches the stress-strain response for the nominal material strength. When accounting for the increased measured strength, the agreement between the two methods was not as pronounced. The effective length associated with the controlling failure mode of cross-section yield was similar, but a more rapid loss of strength was observed with the design procedures with increasing effective length. In both instances, the largest variations were observed around 50% of the yield stress.

As noted previously, flexural-torsional buckling was observed to some degree in all specimens, as would be expected with an asymmetric cross section. However as indicated in Fig. 14, there is a negligible difference in design between the flexural-torsional and the flexural buckling capacities at longer lengths as the response is dominated by the weak-axis flexural buckling failure. A significant variation between the flexural-torsional and flexural behavior is captured at short lengths due to considering a reduced shear stiffness with torsional buckling. Accounting for a constant shear stiffness under compression, line 'Tan. AISC 370 w/ $\tau_G = 1$', significantly increases the flexural-torsional buckling capacity. The increased capacity is a negligible reduction from the flexural buckling capacity across all lengths for this cross section.

Table 5 compares the experimental results to the current design provisions evaluated using the nominal material properties, $P_{d,nom}$, and using the measured material properties, $P_{d,meas}$. The design flexural-torsional buckling capacity was observed to consistently underestimate the experimental results, which is in agreement with previous research on equal-leg angles (Zhang, Tan, and Zhao, 2019; Sarquis et al., 2020; Dobrić et al., 2020; Behzadi-Sofiani, Gardner, and Wadee, 2021; Filipović, Dobrić, Baddoo, et al., 2021; Filipović, Dobrić, Buđevac, et al., 2021). When considering the nominal strength, the design capacities associated with significant torsion were consistently 50% of the observed loads. The consideration of the measured material properties improved the results, but they were still excessively conservative for short columns. The flexural buckling design capacities were also found to conservatively predict the experimental results with improved estimates of the short column behavior. Future work entails an additional series of experiments to confirm the results. Additionally, finite element model validation is underway as part of a parametric study to provide information on various unequal-leg cross sections. This information will then be used to assess if the existing provisions are conservative for unequal-leg single angles in general.

4. Conclusions

This paper presents the experimental results of a series of stainless steel unequal-leg angles subjected to concentric compression. A total of 10 hot-rolled 3" x 2" x ¼" stainless steel angles of varying lengths were tested under axial compression up to failure. Prior to testing, geometric imperfections were measured, and during the experiments, displacement and twist information was recorded along the full length of the member at quarter point intervals. This data was then analysed

to obtain the full behavior of each specimen and to compare the failure modes across the various lengths. The results were compared to the current design provisions for compression members, once considering flexural-torsional buckling, and then neglecting flexural-torsional buckling. It was found that the measured material properties are significantly higher than nominal values, and that this had a significant affect on the capacity predicted by the design provisions. Overall, the results of this study indicated a significant underestimation in the buckling capacity of unequal-leg stainless steel angles. Additional experiments are in progress to expand the test database.

Acknowledgements

References

AISC (2016). *Specification for Structural Steel Buildings ANSI/AISC 360-16*. Chicago, IL: American Institute of Steel Construction, p. 676.

AISC (2021). *Specification for Structural Stainless Steel Buildings ANSI/AISC 370-21*. Chicago, IL: American Institute of Steel Construction, p. 376.

Arrayago, I., E. Real, and L. Gardner (2015). "Description of stress–strain curves for stainless steel alloys". In: *Materials & Design* 87, pp. 540–552. DOI: https://doi.org/10.1016/j.matdes.2015.08.001.

Artec 3D (2020). *Artec Studio 15*. L-2328, Luxembourg: Artec 3D.

ASTM (2016). *Standard Test Methods for Tension Testing of Metallic Materials*. ASTM E8/EM8-16a. West Conshohocken, PA: American Society for Testing and Materials.

Baddoo, Nancy R. (2013). *Structural Stainless Steel*. Design Guide 27. Chicago, IL: American Institute of Steel Construction, p. 150.

Behzadi-Sofiani, Behnam, Leroy Gardner, and M. Ahmer Wadee (2021). "Stability and design of fixed-ended stainless steel equal-leg angle section compression members". In: *Engineering Structures* 249, p. 113281. DOI: 10.1016/j.engstruct.2021.113281.

de Menezes, Arthur A., Pedro C. G. da S. Vellasco, Luciano R. O. de Lima, and André T. da Silva (2019). "Experimental and numerical investigation of austenitic stainless steel hot-rolled angles under compression". In: *Journal of Constructional Steel Research* 152, pp. 42–56. DOI: 10.1016/j.jcsr.2018.05.033.

Dinis, Pedro B., Dinar Camotim, Kostas Belivanis, Colter Roskos, and Todd A. Helwig (2015). "On the buckling, post-buckling and strength behavior of thin-walled unequal-leg angle columns". In: *Proceedings of the 2015 SSRC Annual Stability Conference*. Nashville, TN: SSRC, pp. 1–15.

Dobrić, Jelena, Aljoša Filipović, Zlatko Marković, and Nancy R. Baddoo (2020). "Structural response to axial testing of cold-formed stainless steel angle columns". In: *Thin-Walled Structures* 156, p. 106986. DOI: 10.1016/j.tws.2020.106986.

Filipović, Aljoša, Jelena Dobrić, Nancy R. Baddoo, and Primož Može (2021). "Experimental response of hot-rolled stainless steel angle columns". In: *Thin-Walled Structures* 163, p. 107659. DOI: 10.1016/j.tws.2021.107659.

Filipović, Aljoša, Jelena Dobrić, Dragan Buđevac, Nenad Fric, and Nancy R. Baddoo (2021). "Experimental study of laser-welded stainless steel angle columns". In: *Thin-Walled Structures* 164. DOI: 10.1016/j.tws.2021.107777.

Galambos, Theodore V (1963). "Inelastic lateral buckling of beams". In: *Journal of the Structural Division* 89.5, pp. 217–242.

Galambos, Theodore V. (1991). "Design of axially loaded compressed angles". In: *Proceedings of the 1991 SSRC Annual Stability Conference: "Inelastic Behavior and Design of Frames"*. Chicago, IL: SSRC, pp. 353–367.

Houska, Catherine (2014). *Designing Stainless Steel Part 1*. Conference Presentation. NASSC: The Steel Conference. Toronto, Canada.

Huang, Yuner and Ben Young (2014). "The art of coupon tests". In: *Journal of Constructional Steel Research* 96, pp. 159–175. DOI: https://doi.org/10.1016/j.jcsr.2014.01.010.

Kitipornchai, S and HW Lee (1986). "Inelastic buckling of single-angle, tee and double-angle struts". In: *Journal of Constructional Steel Research* 6.1, pp. 3–20.

Kuwamura, Hitoshi (2003). "Local buckling of thin walled stainless steel members". In: *Steel Structures* 3, pp. 191–201.

Liao, KY (1982). "Compression tests of unequal-leg angles". MA thesis. Ohio State University.

Liu, Yi and Sabine Chantel (2011). "Experimental study of steel single unequal-leg angles under eccentric compression". In: *Journal of Constructional Steel Research* 67.6, pp. 919–928. DOI: 10.1016/j.jcsr.2011.02.005.

Meza, Francisco J., Nancy Baddoo, and Leroy Gardner (2021). "Development of Flexural Buckling Rules for the New AISC Stainless Steel Design Specification". In: *ce/papers* 4, pp. 1537–1542. DOI: https://doi.org/10.1002/cepa.1453.

Neal, B. G. (1950). "The lateral instability of yielded mild steel beams of rectangular cross-section". In: *Philosophical Transactions of the Royal Society of London. Series A, Mathematical and Physical Sciences* 242.846, pp. 197–242. DOI: 10.1098/rsta.1950.0001.

Ojalvo, Morris (2011). "Opposing Theories and the Buckling Strength of Unequal-Leg Angle Columns". In: *Journal of Structural Engineering* 137.10, pp. 1104–1106. DOI: 10.1061/(ASCE)ST.1943-541X.0000389.

Reynolds, Nicholas A. (2013). "Behavior and Design of Concentrically Loaded Duplex Stainless Steel Single Equal-Leg Angle Struts". PhD Dissertation. Georgia Institute of Technology, p. 253.

Sarquis, Fernando R., Luciano R. O. de Lima, Pedro C. G. da S. Vellasco, and Monique C. Rodrigues (2020). "Experimental and numerical investigation of hot-rolled stainless steel equal leg angles under compression". In: *Thin-Walled Structures* 151, p. 106742. DOI: 10.1016/j.tws.2020.106742.

Sippel, Edward J., Ronald D. Ziemian, and Hannah B. Blum (2022). "Buckling behavior of open-web steel joists and joist girders". In: *Proceedings of the 2022 SSRC Annual Stability Conference*. Denver, CO: SSRC, pp. 1–21.

Sun, Yao, Zhanke Liu, Yating Liang, and Ou Zhao (2019). "Experimental and numerical investigations of hot-rolled austenitic stainless steel equal-leg angle sections". In: *Thin-Walled Structures* 144, p. 106225. DOI: `10.1016/j.tws.2019.106225`.

Trahair, Nicholas S and Sritawat Kitipornchai (1972). "Buckling of inelastic I-beams under uniform moment". In: *Journal of the Structural Division* 98.11, pp. 2551–2566.

Wu, Fu-hsiang (1982). "Experimental Determination of Buckling Loads for Unequal Leg Angles with Concentric Loads". MA thesis. Ohio State University.

Zhang, Lulu, Kang Hai Tan, and Ou Zhao (2019). "Experimental and numerical studies of fixed-ended cold-formed stainless steel equal-leg angle section columns". In: *Engineering Structures* 184, pp. 134–144. DOI: `10.1016/j.engstruct.2019.01.083`.

Zhang, Ying, Yidu Bu, Yuanqing Wang, Zhongxing Wang, and Yuanwen Ouyang (2021). "Study of flexural–torsional buckling behaviour of 6061-T6 aluminium alloy unequal-leg angle columns". In: *Thin-Walled Structures* 164, p. 107821. DOI: `10.1016/j.tws.2021.107821`.

Zhang, Ying, Yuanqing Wang, Zhongxing Wang, Yidu Bu, Shenggang Fan, and Baofeng Zheng (2020). "Experimental investigation and numerical analysis of pin-ended extruded aluminium alloy unequal angle columns". In: *Engineering Structures* 215, p. 110694. DOI: `10.1016/j.engstruct.2020.110694`.

Zhang, Ziqian, Gang Shi, Lintao Hou, and Le Zhou (2021). "Geometric dimension and imperfection measurements of box-T section columns using 3D scanning". In: *Journal of Constructional Steel Research* 183, p. 106742. DOI: `10.1016/j.jcsr.2021.106742`.